

1 **Contrasting Aerosol Mixing States at Inland and Coastal Sites: An**
2 **Entropy-Based Metric for CCN Activity**

3 Jingye Ren^{1,2}, Wei Xu³, Ru-Jin Huang^{1*}, Fang Zhang^{4*}, Ying Wang¹, Lu Chen⁵, Jurgita
4 Ovadnevaite⁶, Darius Ceburnis⁶, Colin O'Dowd⁶, Yele Sun⁷

5 ¹*State Key Laboratory of Loess Science, Institute of Earth Environment, Chinese*
6 *Academy of Sciences, Xi'an, 710061, China,*

7 ²*Xi'an Institute for Innovative Earth Environment Research, Xi'an, 710061, China,*

8 ³*State Key Laboratory of Advanced Environmental Technology, Institute of Urban*
9 *Environment, Chinese Academy of Sciences, Xiamen, 361021, China,*

10 ⁴*School of Ecology and Environment, College of Artificial Intelligence, Harbin Institute*
11 *of Technology, Shenzhen, 518005, China,*

12 ⁵*School of Ocean and Geographic Science, Yancheng Teachers University, Yancheng*
13 *224051, China,*

14 ⁶*School of Natural Sciences, Centre for Climate & Air Pollution Studies, Ryan Institute,*
15 *University of Galway, University Road, Galway, Ireland,*

16 ⁷*State Key Laboratory of Atmospheric Boundary Layer Physics and Atmospheric*
17 *Chemistry, Institute of Atmospheric Physics, Chinese Academy of Sciences, Beijing*
18 *100029, China.*

19 Corresponding author: Ru-Jin Huang, rujin.huang@ieecas.cn; Fang Zhang,
20 zhangfang2021@hit.edu.cn

21

22

23

24

25 **Abstract**

26 Simplified assumptions of aerosol mixing states in modeling ~~studies~~ often
27 introduce substantial uncertainties in estimating cloud condensation nuclei (CCN)
28 concentrations (N_{CCN}) and their climatic impacts. This study systematically investigates
29 the contrasting relationships between mixing states and CCN activity by combining
30 field measurements of ~~the hygroscopicity distribution~~ with the algorithm of entropy at
31 two inland and coastal sites. We show distinct seasonal variations of ~~aerosol~~ mixing
32 state. In winter, externally-mixed particles dominated both sites, with comparable
33 mixing state indices (χ) of 0.38 ± 0.12 and 0.39 ± 0.09 respectively for coastal ~~air~~ and
34 inland air. However, measurements ~~during~~ in summer ~~periods~~ showed pronounced
35 differences: aerosols in the coastal atmosphere exhibited a higher degree of internal
36 mixing ($\chi = 0.69 \pm 0.19$), whereas inland χ values only increased moderately to 0.47 ± 0.12 .
37 Aerosol mixing state is largely influenced by primary emissions and secondary
38 formation process. Externally-mixed particles originate chiefly from anthropogenic
39 emissions in inland or sea salt in coastal. ~~During~~ With the aging process, particles
40 become more internally-mixed as the enhanced fraction of more-hygroscopic mode. ~~A~~
41 ~~universal logarithmic correlation was identified~~ Both environments show the negative
42 correlations between the critical diameter (D_{cri}) ~~characterizing CCN activity~~ and χ (~~D_{cri}~~
43 ~~$= -32.15 \ln(\chi) + 84.71$, Pearson $r = -0.74$), but with distinct decrement rates for coastal
44 vs. inland aerosols. Specially, D_{cri} exhibits heightened sensitivity to fluctuations in χ
45 when $\chi < 0.5$. This offers a practical approach to estimate D_{cri} from χ when the particles~~

46 ~~are not highly aged.~~ Further analysis reveals ~~the covariation relationships between the~~
47 ~~mixing state and CCN activity: that~~ N_{CCN} exhibits heightened sensitivity to fluctuations
48 in χ at low values. These results underscore that mixing states exert different control
49 over N_{CCN} in diverse environments. ~~Our work provides and provide~~ critical constraints
50 for parameterizing fine aerosols CCN activity in ~~climate~~ models.

51 **1. Introduction**

52 Atmospheric cloud condensation nuclei (CCNs) are complex mixtures of organic
53 and inorganic components. Their chemical and physical properties make quantifying
54 aerosol-cloud interactions challenging (Liu et al., 2018; Rosenfeld et al., 2019; Xu et
55 al., 2022, 2024; Virtanen et al., 2025), introducing uncertainties into climate effect
56 assessments (Charlson et al., 1992; Shrivastava et al., 2017; IPCC, 2021; Chen et al.,
57 2022a; Manavi et al., 2025). Accurate climate model predictions of aerosol impacts
58 require understanding aerosol mixing states under different atmospheric conditions and
59 their effects on CCN activity (Ching et al., 2016; Zheng et al., 2021a). Current models
60 often oversimplify mixing states by assuming pure internal or external mixing (Winkler,
61 1973; Stevens et al., 2019; Riemer et al., 2019; Zheng et al., 2021b). This is problematic
62 because mixing states directly determine particle hygroscopicity distribution and CCN
63 estimates (Wang et al., 2010; Tao et al., 2024). For example, internal-mixed aerosol
64 particles have unimodal hygroscopicity distribution, while the external-mixed particles
65 are characterized by the bimodal/trimodal or partly overlapping structures (Spitieri et
66 al., 2023; Liu et al., 2025). Such simplifications can lead to significant errors, e.g.,
67 Sotiropoulou et al. (2007) found that mixing state assumptions caused two-fold N_{CCN}

68 estimation errors in global models.

69 Systematic observations across diverse environments are critical because aerosol
70 mixing states exhibit pronounced spatial-temporal variations (Ye et al., 2018; Hughes
71 et al., 2018; Liu et al., 2025). For example, continental and coastal regions present
72 contrasting scenarios (Ramachandran et al., 2016). The continental areas are dominated
73 by anthropogenic emissions, where aerosol aging is driven by industrial and traffic-
74 related pollutants (Huang et al., 2014; Ren et al., 2023). Particles here undergo
75 progressive internal mixing via photochemical process and heterogenous reactions,
76 altering their hygroscopic properties (Ervens et al., 2010; Tao et al., 2021). While the
77 coastal regions feature dynamic interactions between marine aerosols (e.g., sea salt) and
78 continental pollutants (Schill et al., 2015; Collins et al., 2013; Cheung et al., 2020).
79 Seasonal shifts in air mass sources (e.g., marine vs. continental dominance) might
80 create unique mixing state patterns (Xu et al., 2020, 2021a). For instance, summer
81 photochemical aging and heterogenous processes in coastal areas can enhance the
82 degree of internal mixing, while winter often retains more external mixing due to the
83 presence of the sea-salt particles with less-hygroscopic organic matter.

84 The continental aerosols influence regional cloud formation, while coastal
85 aerosols may provide insights into the characteristics of marine aerosols in region. The
86 properties of marine aerosols are significantly different from those of continental
87 aerosols, and therefore have distinct climate feedback mechanisms (Bellouin et al.,
88 2020; Xu et al., 2024; Liu et al., 2024). However, the current models lack regional-
89 specific mixing state parameters and usually assume uniform mixing in both

90 environments. This could lead to large uncertainties in predicting CCN concentrations,
91 highlighting the need for site-specific observations. For example, Ren et al. (2018)
92 found that the impact of aerosol mixing state on CCN activation characteristics ranged
93 from -34% to +16 % in urban atmosphere. Comparison between a fully internal mixture
94 assumption and using the mixing state index from the particle-resolved model, Ching
95 et al. (2017) found the obvious overestimation in CCN concentration ~~estimation~~.
96 Especially in the regions eg., Amazon Basin, Central Africa and Indonesia, the particles
97 appeared to be more external, errors in CCN concentration would increase up to 100%
98 (Hughes et al., 2018). A detailed exploration of mixing state on CCN concentration in
99 global scale was conducted by Zheng et al. (2021a), and the results showed that the
100 mixing state varied spatially with more externally mixed over the North Atlantic Ocean,
101 off the coasts of Southern Africa, and Australia. Thus, assuming particles with
102 internally-mixed would introduce errors in CCN concentration of 50-100%.

103 Therefore, for quantifying the aerosol mixing state in the ambient atmosphere,
104 we apply the algorithm of entropy proposed by Riemer and West (2013) to investigate
105 the aerosol heterogeneity. This index has been applied to quantify the mixing state more
106 reasonably both in field campaigns (Zhao et al., 2021; Yuan et al., 2023) and model
107 simulations (Ching et al., 2016; Zheng et al., 2021a). However, most studies focused
108 on quantifying the particle heterogeneity in composition (Ching et al., 2019; Fierce et
109 al., 2020; Zhao et al., 2021). Here we concentrated on evaluating the heterogeneity in
110 aerosol hygroscopicity for sub-micron particles, which directly related to CCN budget.
111 By refereeing to Yuan et al. 2023, the heterogeneity in hygroscopicity was investigated

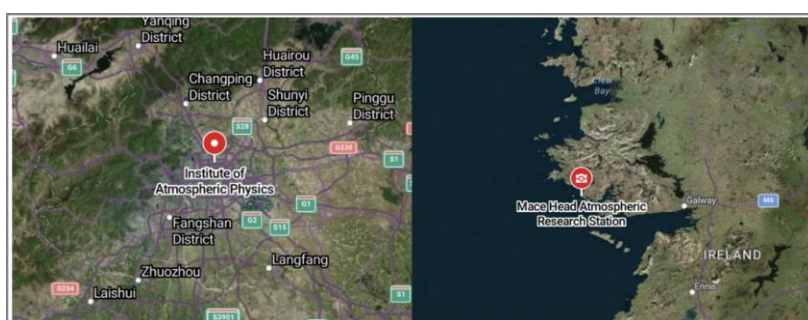
112 by combining in-situ measurements of probability distribution function of the
113 hygroscopicity with the algorithm of entropy. Briefly, the mixing state index χ , is
114 devised based on the concept of information entropy concerning the distribution of
115 hygroscopicity across the aerosol population. It varies between 0 (external mixing
116 completely) and 1 (internal mixing completely). By integrating inland and coastal
117 measurements, this study will focus on addressing two key gaps, (1) How continental
118 vs. marine-dominated environments shape aerosol mixing states and CCN activity; (2)
119 Whether χ -based CCN parameterizations show regional dependencies, providing
120 critical constraints for climate models.

121 **2. Data and Methods**

122 **2.1 Field Campaigns**

123 The inland atmospheric measurements were conducted for two campaigns from
124 16 November to 6 December 2016 and 29 May to 13 June 2017 as a part of the Air
125 Pollution and Human Health (APHH) project (Shi et al., 2019), at the Institute of
126 Atmospheric Physics, Chinese Academy of Sciences (IAP, 39.97° N, 116.37° E) in
127 urban Beijing. The campaigns were complemented by the hygroscopicity and CCN
128 observations and were conducive to provide information on the aerosol hygroscopicity
129 affecting urban pollutions. This urban site exhibited highly variable aerosol populations
130 dominated by local anthropogenic sources including vehicular, cooking emissions, and
131 residential heating. Coastal measurements were performed at the Mace Head
132 atmospheric research station (MHD, 53.33° N, 9.90° W) from 1 November 2009 to 30

133 January 2010, and summer periods from 11 to 31 August 2009 and July 2010, which
134 located on the west coast of Ireland. Aerosol particles here experience alternating
135 influences from polluted continental and clean marine atmospheres. The map of the
136 sites was shown in Figure 1. More details about the campaigns were given in Fan et al.
137 (2020) and Xu et al. (2021a).



138
139 **Fig 1.** Map of the sites in the Inland of the Institute of Atmospheric Physics (IAP) and
140 Coastal of Mace Head (MHD). (© Google Maps, <https://maps.google.com/>, last access:
141 2 April 2025).

142 2.2 Instrumentation

143 Hygroscopicity measurements

144 The particle hygroscopicity at both sites was characterized using the humidified
145 tandem differential mobility analyzer (HTDMA). The hygroscopic growth factor (Gf),
146 defined as the ratio of the particle diameter at the fixed RH (90%) and dry diameter set
147 in this study for 40, 80, 110, 150, 200 nm at IAP and 35, 50, 75, 110 and 165 nm at
148 MHD, respectively. The RH calibration with ammonium sulfate for HTDMA system
149 was given in Fig. S1. The Gf probability density function (Gf-PDF) was derived using

150 the TDMA_{inv} algorithm (Gysel et al., 2009). The number fraction (NF) of near-
 151 hydrophobic mode (NH: $Gf \leq 1.21$), and more hygroscopic mode (MH: $Gf > 1.21$) in
 152 IAP site was referred from Chen et al. (2022b). It was integrated into three modes for
 153 the MHD site with the near-hydrophobic mode (NH: $1 < Gf < 1.3$), more hygroscopic
 154 mode (MH: $1.3 \leq Gf < 1.85$) and sea salt mode (SS: $Gf \geq 1.85$) for further examination
 155 (Xu et al., 2021a).

156 Here for each particle size, the hygroscopicity parameter κ can be subsequently
 157 calculated using κ -Köhler theory (Petters and Kreidenweis, 2007):

$$158 \quad \kappa = (Gf^3 - 1) \cdot \left[\frac{1}{RH} \exp\left(\frac{4\sigma_s M_w}{RT\rho_w D_d Gf}\right) - 1 \right] \quad (1)$$

159 where RH is the HTDMA relative humidity (90% set in the instrument), $\sigma_{s/a}$ is the
 160 surface tension of pure water (0.072 ~~mN~~ m^{-1}), M_w and ρ_w are the molecular weight
 161 and the density of pure water, R is the gas constant, and T is the absolute temperature,
 162 D_d is the droplet diameter.

163 Then, the κ -PDF is obtained and normalized as $\int_0^\infty c(\kappa)d\kappa = 1$, where $c(\kappa)$ is
 164 normalized as κ -PDF. Further it was used to calculate the particle population
 165 heterogeneity (Calculation seen in Section 2.3).

166 According to the κ -Köhler theory, the critical diameter (D_{cri}) corresponding to the
 167 supersaturation ratio can be expressed as:

$$168 \quad D_{cri} = \sqrt[3]{\frac{4A^3}{27\kappa \ln^2 S}}, \quad A = \frac{4\sigma_s M_w}{RT\rho_w} \quad (2)$$

169 where S is the given supersaturation ratio (here 0.2% used in this study), κ is the mean
 170 value of the hygroscopicity parameter calculated in Equation (1).

171 **Chemical components**

172 For the inland atmospheric measurements, the non-refractory submicron aerosol
173 (smaller than $1\mu\text{m}$, NR- PM_{10}) chemical composition was quantitatively characterized
174 using the Aerodyne High-Resolution Time-of-Flight Aerosol Mass Spectrometer (HR-
175 ToF-AMS) (DeCarlo et al., 2006), including sulfate (SO_4^{2-}), nitrate (NO_3^-), ammonium
176 (NH_4^+), chloride (Cl) and organics (Org). The black carbon (BC) mass concentration
177 was determined from the light absorption with a seven-wavelength aethalometer (AE33,
178 Magee Scientific Corp.).

179 Measurements of PM_{10} in the coastal atmosphere were also performed by the HR-
180 ToF-AMS, including major inorganic salts (non-sea-salt sulfate, nss- SO_4^{2-} ;
181 methanesulfonic acid, MSA; NO_3^- ; NH_4^+) and organic matter. The sea salt was
182 quantified using NaCl ion signal, which has been demonstrated in previous studies
183 (Ovadnevaite et al., 2014). The instrument operation and calibration have been
184 described in previous studies (Ovadnevaite et al., 2014; Xu et al., 2019).

185 **Aerosol number size distribution and CCN number concentration**

186 Particle number size distributions (PNSD) were measured using an integrated
187 system consisting of a Differential Mobility Analyzer (DMA; model 3081, TSI Inc.)
188 coupled with a Condensation Particle Counter (CPC; model 3772, TSI Inc.). During the
189 measurements at IAP, the PNSD covered the size range of 10-550 nm with a 5-minute
190 time resolution. It scanned size range of 20-500 nm at MHD with a 10-minute temporal
191 resolution. The CCN number concentrations were quantified at both sites using a
192 Droplet Measurement Technologies CCN counter (DMT-CCNc) (Lance et al., 2006).
193 The instrument's supersaturation (SS) settings were carefully calibrated before and after

194 each campaign using ammonium sulfate aerosol following Rose et al. (2008) (Fig. S1).
195 Four effective supersaturations (SS) were 0.14%, 0.23%, 0.40% and 0.76% at IAP site.
196 Four SS levels were 0.25%, 0.5%, 0.75% and 1% at MHD site with an uncertainty of
197 $\pm 0.03\%$. Using measurements at set supersaturation of 0.2% as an example explores the
198 CCN activity in the following discussions.

199 **2.3 Calculation the heterogeneity for aerosol particles**

200 To characterize the heterogeneous distribution of the hygroscopic and non-
201 hygroscopic components in populations (Chen et al., 2022b), we calculated the mixing
202 state index (χ) using the κ -PDF, following the methodology of Yuan et al. (2023). Two
203 surrogate groups in a population of N aerosol particles were assumed (Zheng et al.,
204 2021a). One surrogate group consists the non- and/or slightly hygroscopic species with
205 κ_N of < 0.05 and another group contains the more hygroscopic species with κ_H of 0.5-
206 0.6 (Yuan et al., 2023, referred inorganics). Ambient particles typically contain one or
207 two of the components and the κ lies between 0 and 0.6 at IAP or 0.8 at MHD as shown
208 in Figure S2. Taking into account the enhanced hydrophilicity of marine aerosols at
209 MHD site, calculation assuming κ_H values of 0.7 and 0.8 were shown in Fig.
210 S3. While these variations in κ_H introduced a mean uncertainty of 8% in χ values, it
211 did not significantly affect the seasonal or site comparisons. The volume fraction of two
212 surrogate groups can be calculated based on the total κ according to the Zdanovskii-
213 Stokes-Robinson (ZSR) mixing rule (Zdanovskii, 1948; Stokes et al., 1966).

214 The mixing state index χ is defined as the affine ratio of the average particle species

215 diversity ($D\alpha$) and population species diversity ($D\gamma$) as:

$$216 \quad \chi = \frac{D\alpha - 1}{D\gamma - 1} \quad (3)$$

217 The average per-particle species diversity $D\alpha$ can be calculated as follows. First,
218 the mixing entropies at bin i (H_i) are determined according to equation (4),

$$219 \quad H_i = -P_{i,N} \times \ln P_{i,N} - P_{i,H} \times \ln P_{i,H} \quad (4)$$

220 where $P_{i,N}$ and $P_{i,H}$ are the volume fraction of each group for the κ -PDF with X bins at
221 bin i ($i=1,2,\dots,X$), and can be determined from the $P_{i,N} + P_{i,H} = 1$ and $P_{i,N} \times \kappa_N +$
222 $P_{i,H} \times \kappa_H = \kappa_i$. Here $\kappa_N = 0.01$, $\kappa_H = 0.6$; κ_i represents the hygroscopicity parameter
223 at bin i .

224 Based on the assumption that particles in the same diameter have the same mixing
225 entropy $H_\alpha = \sum_{j=1}^N P_j \times H_j$, $P_j = \frac{V_j}{V_{total}} = \frac{1}{N}$; the per-particle mixing entropies H_α is
226 determined according to equation (5),

$$227 \quad H_\alpha = \sum_{i=1}^X H_i \times c(\kappa)_i \times \Delta\kappa \quad (5)$$

228 where $c(\kappa)_i$ is the probability density of the normalized κ -PDF at bin i , and $\Delta\kappa$
229 represents the bin width. Then, the average per-particle species diversity $D\alpha$ can be
230 determined as $D\alpha = e^{H_\alpha}$;

231 The bulk population species diversity $D\gamma$ can be calculated as follows. First, the
232 aerosol population of the mixing entropy can be calculated as equation (6):

$$233 \quad H_\gamma = -P_N \times \ln P_N - P_H \times \ln P_H \quad (6)$$

234 where P_N and P_H are the volume fraction of the non-hygroscopic and hygroscopic
235 components in the population, and can be calculated by equation (7) and (8):

$$236 \quad P_N = \sum_{i=1}^X P_{i,N} \times c(\kappa)_i \times \Delta\kappa \quad (7)$$

237
$$P_H = \sum_{i=1}^X P_{i,H} \times c(\kappa)_i \times \Delta\kappa \quad (8)$$

238 Then, the bulk population species diversity D_γ can be determined as $D_\gamma = e^{H_\gamma}$.

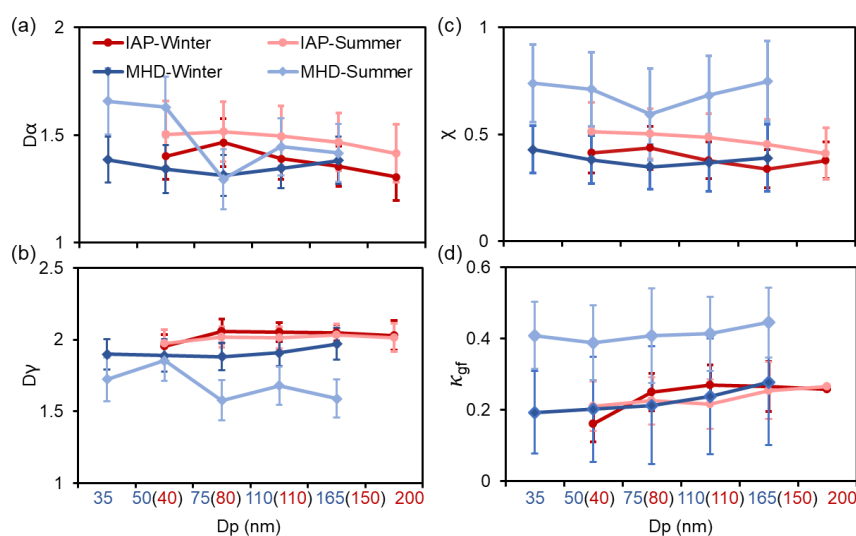
239 Here, the definition of surrogate species as supersets encompassing hygroscopicity
240 heterogeneity implies that the heterogeneity parameter χ ranges from 0 to 1. When the
241 mixing index χ approaches 0, it indicates a completely segregated state where
242 hygroscopic and non-hygroscopic species reside in distinct particles. ~~While for~~ For the
243 case ~~where~~ the mixing index χ ~~to be~~ is 1, it represents ~~that the~~ homogeneous distribution
244 ~~of~~ non-hygroscopic and hygroscopic species ~~distributing homogeneously~~ throughout
245 the aerosol population.

246 3. Result and Discussion

247 3.1 Comparison of the heterogeneity in the inland and coastal atmosphere

248 To characterize the hygroscopic heterogeneity of atmospheric aerosols, Figure 2
249 depicts variations in mixing state metrics (D_α , D_γ , χ) and the hygroscopic parameter
250 (κ_{gf}) across particle size distributions. The D_α and χ decrease with increasing particle
251 diameter, accompanied by higher κ_{gf} values at IAP site. This trend indicates that inland
252 particle populations tend to homogenize into hygroscopic compositions through
253 primary particle aging or secondary formation processes (Liu et al., 2025; Chen et al.,
254 2022b; Zhong et al., 2022). In contrast, particles exhibit a non-monotonic pattern at
255 MHD site: D_α and χ decrease for Aitken-mode particles (<100 nm) but increase for
256 accumulation-mode particles. The κ_{gf} shows consistent size-dependent increases in
257 both winter and summer campaigns.

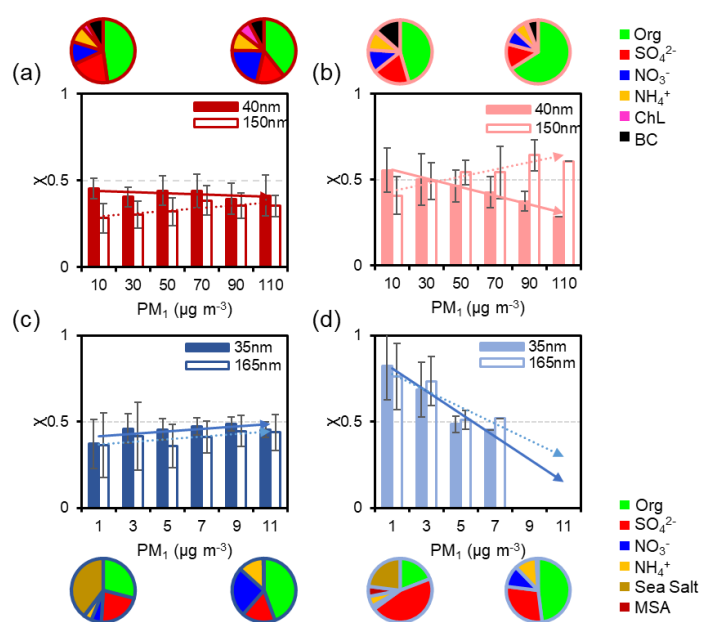
258 Notably, the mixing state metrics exhibit a pronounced minimum at 75 nm
 259 particles, influenced by distinct mechanisms: winter minima reflect the high sea salt
 260 fraction, while summer minima are driven by anthropogenic organic matter (Cheung et
 261 al., 2020; Xu et al., 2021a). Lower winter χ values—coupled with broader κ -PDF
 262 distributions—indicate stronger external mixing and compositional diversity compared
 263 to summer (Fig. S2). Seasonal χ and κ_{gf} disparities are more pronounced at MHD site,
 264 primarily driven by the seasonal alternation of marine and anthropogenic emission
 265 sources.



266
 267 **Fig 2.** Mean values of the $D\alpha$ (a), $D\gamma$ (b), χ (c) and κ_{gf} (d) for aerosols of five diameters
 268 during winter and summer periods at IAP and ~~Mace Head~~MHD sites.

269 Ultrafine particles (40 nm in IAP vs. 35 nm in MHD, Aitken mode) and larger
 270 particles (150 nm in IAP vs. 165 nm in MHD, accumulation mode) are selected to
 271 investigate distinct evolutionary processes of aerosol heterogeneity (Fig. 3 and Fig. S4).

272 With the increasing of PM₁ concentration during winter, the variation in χ values exhibit
 273 only minor both at the IAP and MHD sites, generally fluctuating between
 274 approximately -0.04 and 0.08 (Fig. 3a and c). Inland accumulation-mode particles
 275 show a modest increase in χ , corresponding with a higher proportion of inorganic salts.
 276 Conversely, at MHD site, the composition fraction shifts from a sea-salt dominance



277 **Fig. 3.** Variation of the average χ for 40 nm and 150 nm particles at IAP and 35 nm and
 278 165 nm at MHD site with the particle mass concentration in IAP-winter (a), IAP-
 279 summer (b), MHD-winter (c) and MHD-summer (d). The pie charts represent the
 280 average mass fraction during four field measurements.

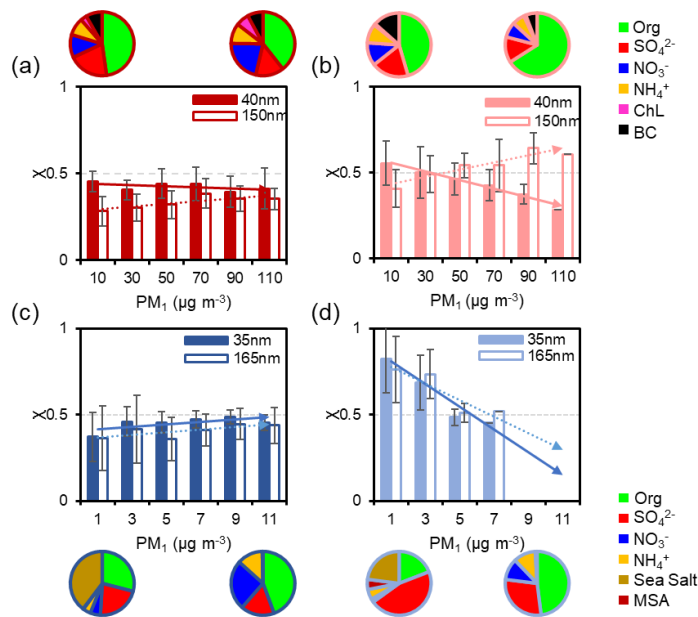
282 toward organic matter, accompanied by a ~20 % increase in nitrate content (Fig.
 283 3c). In summer, the variation of χ with PM concentration becomes markedly
 284 pronounced at both IAP and MHD stations. For example, χ for 40 nm particles

带格式的: 缩进: 首行缩进: 2 字符

285 decreases as PM increases at IAP site (Fig. 3b). The elevated particle heterogeneity
286 mainly arises from the locally primary emissions, corresponding to the enhanced
287 primary organic emissions as shown in Fig. S5. It appeared more pronounced during
288 evening rush hours. In contrast, χ for 150 nm particles increases from ~ 0.40 to ~ 0.60
289 with rising PM, reflecting enhanced secondary formation and internal mixing during
290 pollution process that render the particle population more homogeneous. At coastal sites,
291 χ declines with rising PM by approximately 0.37 for 35 nm particles and 0.24 for
292 165 nm particles, mirroring the shift in chemical composition makeup from inorganic
293 dominance to greater organic content (Fig. 3d).

294 Diurnal variations of mixing state metrics ($D\alpha$, $D\gamma$, Gf-PDF and χ) at IAP and
295 MHD sites are shown in Figure 4. In IAP-winter, particles exhibited steeper declines in
296 $D\alpha$ and χ during evening rush hours than summer, indicating a higher fraction of non-
297 hygroscopic particles (40 nm) from fresh traffic emissions (Fig. 4a1 and S5).
298 Concurrently, reduced $D\gamma$ values suggest that the bulk population consists of uniformly
299 distributed less-hygroscopic (LH) components (Fig. 4c1). Aitken mode particles
300 showed bimodal and broader Gf-PDF distributions, corresponding to cooking activities
301 (11:00–13:00 LT) and traffic peaks (17:00–20:00 LT) (Cai et al., 2020). Midday
302 photochemical aging promoted more internally mixed aerosols (Yang et al., 2012; Liu
303 et al., 2025), as evidenced by increasing $D\alpha$ at the urban site (Fig. 4b1). Conversely, the
304 χ for accumulation-mode particles showed minimal diurnal variations both in IAP-
305 winter and IAP-summer. This is mainly due to the dominant hygroscopic mode for 150
306 nm particles (Fig. 4g1 and 4h1), especially during summer, which is mainly from

307 secondary formation or aging of the primary particles (such as the transformation from
 308 primary organic aerosol (POA) to secondary organic aerosol (SOA) in Fig. S5) (Wang
 309 et al., 2019; Fan et al., 2020).

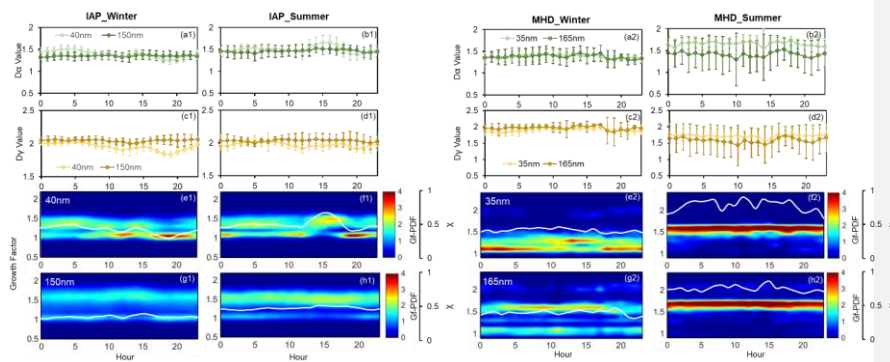


310
 311 **Fig 3.** Variation of the average γ for 40 nm and 150 nm particles at IAP and 35 nm and
 312 165 nm at MHD site with the particle mass concentration in IAP-winter (a), IAP-
 313 summer (b), MHD-winter (c) and MHD-summer (d). The pie charts represent the
 314 average mass fraction during four field measurements.

315 For the coastal atmosphere, the mixing state metrics ($D\alpha$, $D\gamma$, and χ) of Aitken and
 316 accumulation mode particles in winter exhibited analogous diurnal patterns,
 317 characterized by a descending trend at nightfall (Fig. 4a2-h2). This corresponds to an
 318 enhanced modal distribution of near-hydrophobic (NH) particles at 35 nm and more-

带格式的: 段落间距段前: 0.5 行

319 hygroscopic (MH) particles at 165 nm. In summer, $D\alpha$ and $D\gamma$ both trended downward
 320 during daytime, with the decline of $D\gamma$ being more pronounced. A conspicuous seasonal
 321 discrepancy between Aitken and accumulation mode particles was observed in this
 322 region (Fig. 4a2–h2), where the mixing state index χ increased incrementally from
 323 winter to summer. Specifically, the mean χ for 35 nm particles escalated from 0.42 to
 324 0.80, and for 165 nm particles, it rose from 0.39 to 0.76. This trend demonstrates a
 325 strong alignment with the spread factor (used as a measure of particle mixing state)
 326 documented by Xu et al. (2021a).



327
 328 **Fig 4.** Diurnal variation of $D\alpha$, $D\gamma$, Gf-PDF, and χ during winter and summer periods
 329 for 40 nm and 150 nm aerosols at IAP (a1-h1) and for 35 nm and 165 nm aerosols MHD
 330 site (a2-h2).

331 Similar to the mixing state χ , a very clear seasonal pattern of the aerosol
 332 hygroscopic distribution was found (Fig. 4e-h). In winter, the Gf-PDF diurnal profiles
 333 of both Aitken and accumulation mode particles showed bimodal distribution (Fig. 4e2-
 334 g2) as evident by the number fraction of nearly-hydrophobic and more hygroscopic

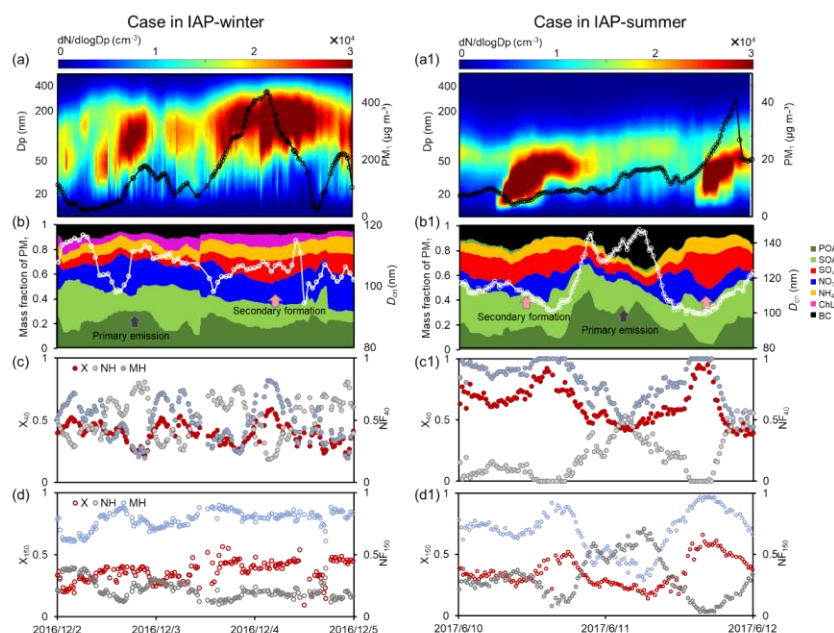
335 modes (Fig. S6). The NH mode is likely composed of anthropogenic organic matter and
336 biogenic species derived from marine air masses (Xu et al., 2020), with this
337 composition being particularly prominent in the Aitken mode. Additionally, Xu et al.
338 (2021a) observed a higher abundance of the NH-mode in marine polar and Arctic air
339 masses, this further supports the notion that NH particles are likely of biogenic origin,
340 aside from contributions from anthropogenic activities. The more hygroscopic and sea
341 salt mode was mostly contributed from the nss-sulfate and sea salt in winter (Xu et al.,
342 2021a). Analogously, accumulation mode particles with a higher proportion of MH and
343 SS mode (Fig. S6) primarily attributed to the prevalence of non-sea-salt sulfate (nss-
344 sulfate) and sea salt in the coastal atmosphere (Xu et al., 2020). The bimodal and broad
345 of hygroscopic distribution suggested that particles were more diverse and external
346 mixed, consistent with the lower χ value in winter.

347 In contrast, summer observations revealed that Gf-PDFs of both Aitken and
348 accumulation mode particles transitioned to unimodal distributions, signifying particles
349 in summer had more homogeneous composition with a large extent of internal mixing
350 particles (with higher χ). Such diurnal trend in Gf-PDFs was consistent along with the
351 high number fraction of MH-mode and low NH-mode (Fig. S6). The higher
352 hygroscopicity and MH mode in summer were largely driven by the enhancement of
353 sulfate and decrease of organic matter (Fig. S6). And a clear shift from NH to MH mode
354 at midday might further demonstrate the promotion of photochemical aging in summer
355 (Xu et al., 2021a).

356 **3.2 Impacts of Primary Aerosol Emissions and Secondary Aerosol Formation on** 357 **Aerosol Mixing State**

358 As already noted above, changes in χ were clearly associated with the chemical
359 composition varying with site and season. The relationships between the mixing state
360 index and the number fraction of hydrophobic and hygroscopic mode during four
361 campaigns are presented in Figure S7. The χ exhibited negative correlations with the
362 fraction of hydrophobic mode but a positive relationship with the fraction of
363 hygroscopic particles, highlighting the markedly different effects of the primary
364 emissions and secondary formation on aerosol mixing state (Tao et al., 2024). To gain
365 more insight on this effect between inland and coastal atmosphere, four case are
366 analyzed (Fig. 5 and 6): case for IAP-winter, case for IAP-summer, case for MHD-
367 winter and case for MHD-summer.

368 Case for IAP-winter is a heavy polluted event with the mean PM mass
369 concentration increased from 22 to 437 $\mu\text{g m}^{-3}$ (Fig. 5a-d). The 40- and 150-nm χ
370 patterns shifted quickly during the pollution periods. With the mass fraction of
371 hydrophobic compounds (ie., POA) in PM_{10} increased, the χ of 40-nm particles
372 decreased from 0.5 to 0.2, that is, an enhanced NH mode and a weakened MH mode (Fig.
373 5b-c). At this stage, large particles for 150 nm are mainly from aqueous formation with
374 more proportion of nitrate. The corresponding χ of 150-nm [particle](#) was higher. While
375 with that the mass fractions of secondary organic and inorganic compositions increased,
376 particles were more internally mixed with χ increased to be 0.6 for 40-nm and 0.53 for
377 150-nm particles.

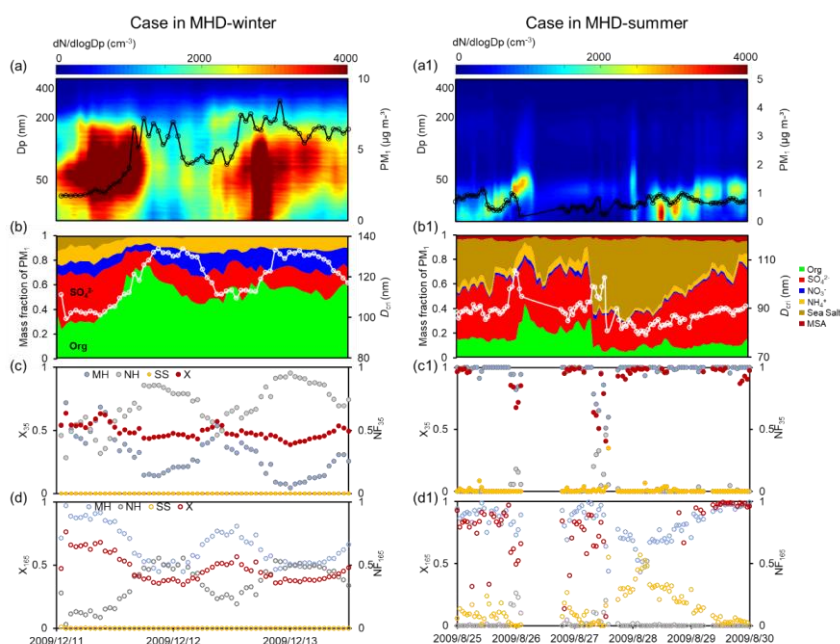


378

379 **Fig 5.** Case in IAP-winter (a-d) and IAP-summer (a1-d1). Particle number size
 380 distribution and PM_{10} (a and a1), mass fraction of the PM_{10} and the critical diameter (D_{crit})
 381 (b and b1), mixing state index (χ), number fraction of the nearly hydrophobic mode
 382 (NH) and more hygroscopic mode (MH) for 40 nm particles (c and c1), χ , NH and MH
 383 for 150 nm particles (d and d1).

384 Case for IAP-summer is the typical new particle formation events (NPF) with the
 385 mean PM_{10} of $13 \mu\text{g m}^{-3}$ (Fig. 5a1-d1). With the evolution of NPF events, the χ of 40-
 386 and 150-nm particles increased to be 0.95 and 0.61 with the enhanced proportion of
 387 more-hygroscopic components (ie., SOA, NO_3^- , SO_4^{2-}). The χ pattern is opposite of that
 388 the number fraction of NH mode and consistent with the variation of MH mode (Fig.
 389 S7). Note that a sudden decrease in χ on June 11th was disturbed by the strong primary

390 emission. The chemical mass fractions showed more POA and black carbon with an
 391 enhanced NH mode and a weaker MH mode (Fig. 5b1-d1). The χ of 40-nm particles
 392 decreased to be 0.4 and that of the 150-nm particles decreased to be 0.2. The χ patterns
 393 appear to similar transitions for Aitken and accumulation-mode particles during haze
 394 and NPF events. The increase in χ is synchronous with the increase in MH mode from
 395 secondary formation but opposite with that of LH mode from primary emissions. This
 396 implies that the primary emissions would lead particles more external mixing while
 397 secondary formation would promote aerosol more internal mixed in Inland atmosphere.



398
 399 **Fig 6.** Case in MHD-winter (a-d) and MHD-summer (a1-d1). Particle number size
 400 distribution and PM_{10} (a and a1), mass fraction of the PM_{10} and the critical diameter (D_{crit})
 401 (b and b1), mixing state index (χ), number fraction of the nearly hydrophobic mode
 402 (NH) and more hygroscopic mode (MH) for 35 nm particles (c and c1), χ , NH and MH

403 for 165 nm particles (d and d1).

404 Case for MHD-winter is a high organic matter pollution event with the mean PM₁
405 of 5.2 $\mu\text{g m}^{-3}$ and 52% mass fraction of organics (Fig. 6a-d). Larger presence of
406 anthropogenic organic matter resulted the NH mode for 35-nm particles to be 95% and
407 165-nm particles to be 53% (Fig. 6). The χ of 35- and 165-nm particles decreased with
408 the NH mode increased (Fig. S7), similar with the case for IAP site. There was a steady
409 increase in χ when the MH-mode particles started increasing with the increase in mass
410 fraction inorganics, eg., 35 nm particles showed the mean χ increasing from 0.43 to
411 0.57 and 165 nm particles from 0.35 to 0.6. This indicated that the trend of aerosol
412 mixing state closely followed the evolution emission and secondary formation.

413 Case for MHD-summer is an extremely clean event with the mean PM₁ of 0.7 μg
414 m^{-3} (Fig. 6a1-d1). The dominated MH mode was found throughout the case, which
415 could be attributed from the high mass fraction of nss-sulfate (41% average). Compared
416 with the case in MHD-winter, the mean proportion of organic has decreased to be 15%.
417 Therefore, the χ remains at a high value (mean χ of 0.9 for 35-nm and 0.8 for 165-nm
418 particles). Until August 28th, a stronger increase in the mass fraction of sea salt and
419 accordingly SS mode in larger-size particles was observed. The χ decreased rapidly
420 with the decrease in MH mode and enhanced SS mode, especially for the accumulation
421 mode particles, suggesting the sea spray production makes particles more externally
422 mixed.

423 In summary, these results suggest that the primary emission and secondary
424 formation drive the hygroscopic distribution and can result in significant variation of

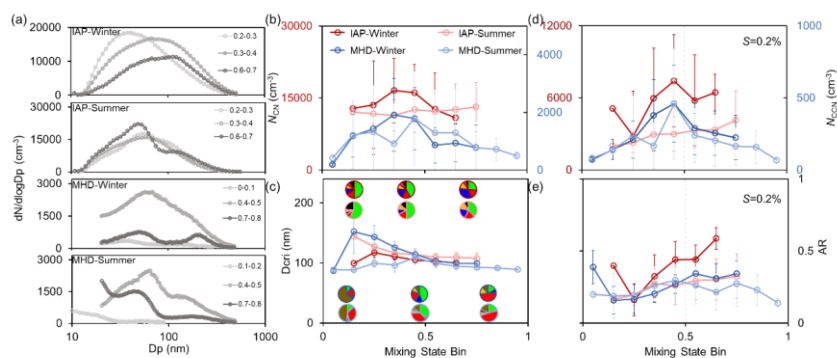
425 aerosol mixing state χ both in Inland and coastal atmosphere. The pattern of χ varied
426 among site and season, highlighting the importance of considering the impact of mixing
427 state on CCN activity.

428 **3.3 Covariation relationships between the Mixing State and CCN Activity**

429 The mixing state of particle populations undergoes dynamic transformations
430 during atmospheric aging, profoundly influencing their CCN activity. Unlike prior
431 CCN closure studies that assumed mixing states based on chemical component
432 fractions (Yang et al., 2012; Padró et al., 2012; Ren et al., 2018), this work employs the
433 hygroscopicity distribution- and entropy-derived mixing state index χ to clarify the
434 covariation relationships between the mixing state and CCN activity. Given that CCN
435 activity reflects the characteristics of the entire particle population while χ is calculated
436 from HTDMA measurements at specific particle diameters, this study chooses the N_{CCN} ,
437 activation ratio (AR) at supersaturation of 0.2% and the mean χ for accumulation-mode
438 to illustrate the covariation characteristic approximately. This approach is employed to
439 ensure that both variables/parameters reflect the characteristics of the accumulation-
440 mode particle population. The covariations of particle size and chemical composition
441 with the mixing state (χ ranging from 0 to 1 at intervals of 0.1) are illustrated in Figure
442 7. This figure provides key insights into two fundamental determinants of CCN activity
443 (Dusek et al., 2006).

444 As χ increases, the peak diameter (D_{peak}) of the particle number size distribution
445 (PNSD) shifts toward larger sizes (Fig. 7a and Fig. S8), while peak concentrations occur

446 within the intermediate χ range (0.3–0.6). This trend indicates that CN number
 447 concentration (N_{CN}) first increases, driven by primary emissions and new particle
 448 formation, then decreases due to mixing and aging processes (Fig. 7b). Notably, new
 449 particle formation events frequently occurred in IAP-summer (Fig. S9), corresponding
 450 the gradually increase of χ . And the χ for Aitken-mode is significantly larger than the
 451 accumulation-mode particles during this period. Thus, N_{CN} exhibits a sustained slight
 452 increase as the degree of the internal mixing increases in IAP-summer.



453
 454 **Fig 7.** Comparison of the average particle number size distribution (PNSD) in different
 455 mixing state index (χ) (a), CN number concentration (N_{CN}) as a function of χ (b),
 456 Critical diameter (D_{crit}) at $S=0.2\%$ and mass fraction of chemical composition as a
 457 function of χ (c), CCN number concentration (N_{CCN}) (d) and activation ratio (AR) at
 458 $S=0.2\%$ a function of χ (e).

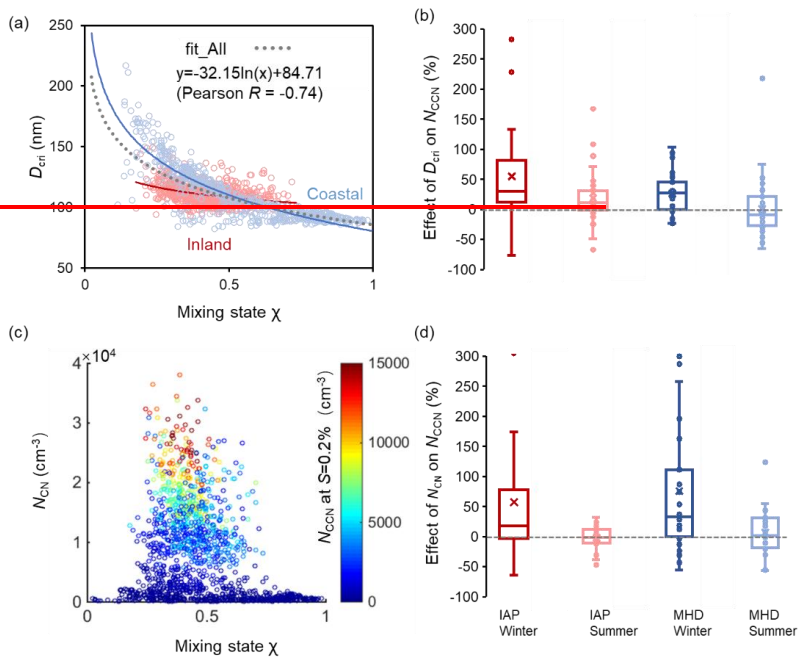
459 The critical diameter (D_{crit})—defined as the minimum size required for activation
 460 at a given supersaturation—depends on aerosol hygroscopicity. In turn, this
 461 hygroscopicity is jointly determined by the hygroscopicity of individual soluble
 462 components and their mass fractions in the aerosol (Petters and Kreidenweis, 2007).

463 Using measurements at supersaturation of 0.2% as an example, Fig. 7c shows that D_{cri}
464 decreases with increasing highly hygroscopic inorganic components (e.g., sulfate,
465 nitrate) in the inland atmosphere. In contrast, coastal D_{cri} exhibits nonlinear variations
466 with χ : high external mixing (low χ) elevates D_{cri} due to dominant organic components,
467 reducing sea salt particle fractions. As χ increases, the mass fraction of non-sea-salt
468 sulfate (nss-sulfate) rises, enhancing activation potential by decreasing D_{cri} .

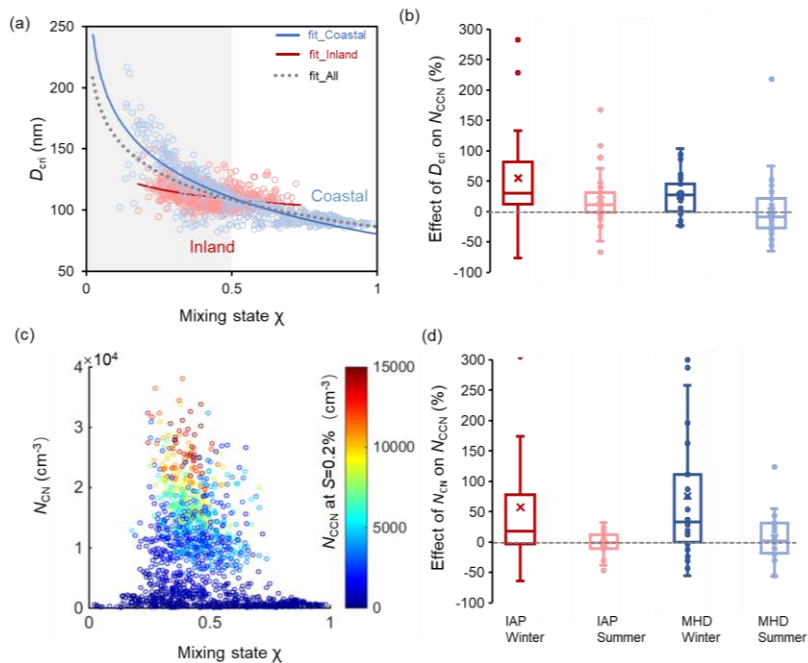
469 The covariation characteristic of CCN activity at 0.2% supersaturation with
470 mixing state index χ reveals distinct inter-atmospheric differences, as shown in Fig. 7d-
471 e. In IAP, N_{CCN} at $S=0.2\%$ demonstrates a monotonic increasing trend with χ , attributed
472 to the synergistic effects of rising N_{CN} and decreasing D_{cri} (Fig. S10). By contrast,
473 coastal N_{CCN} follows a pattern analogous to N_{CN} , with peak concentrations shifting
474 toward higher χ values. This highlights the dominant role of particle size effects in
475 enhancing CCN concentrations under marine-influenced conditions (Dusek et al.,
476 2006).

477 Two distinct $D_{\text{cri}}-\chi$ trends underpin these disparities: one remains stable, driven by
478 the inherent hygroscopicity of sea salt, while the other exhibits steep D_{cri} declines
479 associated with anthropogenic pollution as internal mixing intensifies. These
480 discrepancies are further manifested in the nonlinear $D_{\text{cri}}-\chi$ relationship. The activation
481 ratio (AR)—quantifying aerosol cloud droplet formation potential at fixed
482 supersaturation—also varies by site (Fig. 7e). Notably, AR shows a marked increase
483 with χ in IAP-winter, likely due to enhanced N_{CCN} from the elevated inorganic fraction
484 under higher mixing states (Fig. 3). Conversely, the inorganic fraction decreases during

485 other sampling periods, dampening AR growth.



486



487

488 **Fig 8.** Covariation characteristics of the critical diameter (D_{cri}) with the χ (a), relative
489 change of CCN number concentration (N_{CCN}) at supersaturation $S = 0.2\%$ with the
490 reduction in D_{cri} (b); Covariation characteristics of the CN number concentration (N_{CN})
491 with the χ , different colors represent the N_{CCN} (c), relative change of N_{CCN} with the
492 change in N_{CN} (d).

493 ~~Fig. 8 further shows~~The mixing state directly reflects the degree of particle aging,
494 ~~which subsequently influences the particle composition and size. Fig. 8 further~~
495 ~~examines~~ the covariation characteristics of CN concentration, chemical compositions
496 (i.e., D_{cri}) with mixing state across particle populations. ~~D_{cri} exhibits heightened~~
497 ~~sensitivity to minor χ fluctuations in the mixing state (χ) when $\chi < 0.5$ (Fig. 8a).~~The
498 ~~mixing state index quantifies the variance in hygroscopic distribution that emerges~~
499 ~~directly from compositional heterogeneity. Thus, it can indirectly affect D_{cri} by serving~~
500 ~~as an indicator of particle aging. The critical diameter (D_{cri}) is intrinsically sensitive to~~
501 ~~the hygroscopic distribution—wherein broader hygroscopic spectra (corresponding to~~
502 ~~lower χ) engender more extensive D_{cri} ranges. As shown in Fig. 8a, the D_{cri} exhibits~~
503 ~~heightened sensitivity to minor χ fluctuations in the mixing state (χ) when $\chi < 0.5$. This~~
504 ~~significant decrease in D_{cri} with increasing χ further confirms the potential effect of~~
505 ~~aging degree on critical particle diameter.~~In contrast, for particles already characterized
506 by internal mixing, further increases in χ (i.e., higher degrees of internal mixing) exert
507 a negligible influence on D_{cri} . ~~Particularly when $\chi > 0.7$, the variation in D_{cri} with χ is~~
508 ~~within 20%. This behavior pattern reflects the influence of hygroscopic heterogeneity~~
509 ~~on critical diameter and might enable a novel parameterization for D_{cri} estimation.~~This

设置了格式: 字体颜色: 自动设置

设置了格式: 字体颜色: 自动设置

设置了格式: 字体颜色: 自动设置

510 behavior pattern implies that the $D_{\text{cri}}-\chi$ relationship could enable a novel
511 parameterization for D_{cri} estimation, ~~a framework that has not yet been reported in the~~
512 ~~existing literature.~~ when the aerosol particles are not highly aged or when the internal
513 mixing degree of aerosol particles is relatively low, serving as a novel framework for
514 integrating mixing state effects on CCN activity in atmospheric models.

设置了格式: 字体颜色: 自动设置

515 Aerosol observation at MHD site (blue dots) span a broad D_{cri} range (80–220 nm)
516 with χ varying from 0.1 to 1, reflecting alternating influences of highly hygroscopic
517 inorganic salts (sea salt, sulfate) and less-hygroscopic organic matter. In contrast,
518 ~~aerosols—observation at IAP site that is dominated by anthropogenic pollutants—~~

设置了格式: 字体颜色: 自动设置

519 ~~aerosols~~ exhibit a narrower D_{cri} range (90–150 nm) ~~at IAP site.~~ Both environments
520 show negative $D_{\text{cri}}-\chi$ correlations, but with distinct functional forms: For instance,
521 MHD aerosols feature an exceptional logarithmic fit ($D_{\text{cri}} = -42.98\ln(\chi) + 80.36$, Pearson
522 $r = -0.87$, $R^2 = 0.75$; Fig. 8a blue line), while IAP aerosols (red line) yield a shallower

设置了格式: 字体颜色: 自动设置

523 slope (-12.04). ~~Pooling all data, we derive a generalized parameterization:~~ and Pearson
524 ~~r of -0.4. This quantifies that $D_{\text{cri}} = -32.15\ln(\text{sensitivity to } \chi) + 84.71$ (Pearson $r = -0.74$,~~
525 ~~$R^2 = 0.54$), is 3.6 times steeper in MHD environments. This behavior pattern implies~~

设置了格式: 字体颜色: 自动设置

设置了格式: 字体颜色: 自动设置

526 that the $D_{\text{cri}}-\chi$ relationship could enable a novel framework for D_{cri} estimation. The
527 slope reflects the compositional diversity of the regime, steeper slopes occur where
528 small χ variations correspond to large compositional shifts (e.g., sea salt in coastal site).

设置了格式: 字体颜色: 自动设置

529 As discussed above, strong impact of primary emission and secondary formation on
530 aerosol mixing state was observed in both sites (Fig. 5 and 6). One could obtain more
531 details on the $D_{\text{cri}}-\chi$ correlations. For example, the D_{cri} exhibited rapidly increase with

532 the increase of primary emissions (ie., mass fraction of POA enhanced) during polluted
533 periods. The D_{cri} pattern appeared opposite with that of the mixing state index,
534 especially for the accumulation-mode particles. More pronounced $D_{\text{cri}}-\chi$ correlations
535 were observed during the new particle formation (Fig. 5a1-d1). The decreasing
536 presence of D_{cri} matched the increasing proportion of SO_4^{2-} and SOA with the χ
537 increased during NPF events. Similar correlations between the critical diameter and
538 mixing state index were also found in the coastal atmosphere, especially for the case of
539 the enhanced anthropogenic organic matter and sea salt production (Fig. 6). This
540 implies that the relationship between the D_{cri} and χ might be disturbed by the variation
541 of emission pollution and secondary formation processes, resulting in spatiotemporal
542 differences. The D_{cri} reduces by 2.2–6.8% with the mixing state increase at a step of
543 0.1, with the steepest winter decline (Fig. S11).

544 Changes in N_{CN} with differ starkly between environments: positive effects in
545 polluted inland air (+9%) versus negative effects in coastal regions (-2%). Aerosols in
546 IAP, frequently perturbed by primary emissions and new particle formation, exhibit
547 elevated N_{CN} (peaking at $\chi = 0.2-0.7$), while in MHD N_{CN} remains $\sim 5000 \text{ cm}^{-3}$ across
548 all χ . We categorized data into two groups: C1 (particles within specific N_{CN} ranges)
549 evaluates N_{CCN} covariations mainly driven by $D_{\text{cri}}-\chi$ relationships, while C2 (particles
550 within fixed D_{cri} intervals) assesses $N_{\text{CN}}-\chi$ effects (Fig. 8b). Relative changes (RC) in
551 D_{cri} , N_{CN} , and N_{CCN} with χ were calculated by comparing successive χ increments (χ_{i+1}
552 vs. χ_i , $i=0,0.1\dots 1$) within defined N_{CN} or D_{cri} windows.

553 Notably, the covariation relationship between the N_{CCN} and mixing state exerts

设置了格式: 字体颜色: 自动设置, 非上标/下标

设置了格式: 字体颜色: 自动设置

设置了格式: 字体颜色: 自动设置, 非上标/下标

设置了格式: 字体颜色: 自动设置

设置了格式: 字体颜色: 自动设置, 非上标/下标

设置了格式: 字体颜色: 自动设置

设置了格式: 字体颜色: 自动设置

554 more pronounced for the case of externally mixed aerosols dominated. For example,
555 MHD-winter aerosols (high external mixing; $\chi_{\text{mean}}=0.38\pm0.12$) showed RCs in N_{CCN} of
556 23% (C1) and 72% (C2), whereas MHD-summer aerosols (high internal mixing;
557 $\chi_{\text{mean}}=0.69\pm0.19$) exhibited negligible effects (-2.5% in C1, 0.9% in C2). Inland
558 atmospheres, despite smaller seasonal χ variations, showed analogous trends: RCs of
559 N_{CCN} in winter (55% in C1, 57% in C2 for external mixing) exceeded summer values
560 for more internally mixed populations (Fig. 8d). These results confirm that hygroscopic
561 heterogeneity strongly influences N_{CCN} under external mixing, aligning with prior work
562 (Ching et al., 2017).

563 The covariation characteristics are most pronounced during winter in both
564 environments, attributed to heightened winter D_{cri} sensitivity to χ : a 0.1 χ increase
565 reduces D_{cri} by 5.2% (winter), boosting N_{CCN} by 39%, versus 2.4% D_{cri} reduction
566 (summer) yielding only 6% N_{CCN} enhancement. Concomitantly, winter $N_{\text{CN}}-\chi$ effects on
567 N_{CCN} reach 65%, far exceeding summer responses.

568 In contrast to previous evaluation methods that oversimplify mixing states (Ren et
569 al., 2018; Xu et al., 2021b), the entropy-based framework employed in this study
570 explicitly characterizes the covariation between the CCN activity and transitions in the
571 mixing state. Aerosols in IAP-winter are presumably shaped by intense urban pollution
572 sources—including traffic emissions, residential heating, and cooking activities—
573 thereby enriching the externally mixed particle fraction (Fan et al., 2020; Xie et al.,
574 2020). Analogously, aerosols in MHD-winter exhibit dominant external mixing,
575 consisting of near-hydrophobic and hydrophilic particle mixtures (Xu et al., 2021a). As

576 illustrated in Fig. S2, the winter aerosol population exhibits bimodal or multimodal κ -
577 PDF distributions—this pattern indicates a high degree of external mixing, with the
578 aerosols characterized by chemically diverse compositions. Collectively, these results
579 underscore the pivotal role of mixing state heterogeneity in modulating CCN activity
580 across different environments.

581 4. Conclusions

582 The mixing state of aerosol populations undergoes complex transformations
583 during atmospheric aging, altering the distribution of hygroscopic and non-hygroscopic
584 components and thus influencing CCN activity (Xu et al., 2021a; Ching et al., 2017).
585 This study derived a mixing state index (χ) from field-measured hygroscopicity
586 distributions, systematically investigating the covariation relationship between the
587 mixing state and CCN activity at two inland and coastal environments. Results provide
588 field evidence that aerosol mixing states generally reside between purely internal and
589 external extremes (Chen et al., 2022b). Aerosol mixing state is largely influenced by
590 the primary emissions and secondary formation process. Externally-mixed particles
591 with more hydrophobic-mode originate chiefly from primary emissions in IAP, while
592 ~~that~~ those of more sea-salt mode from sea spray in MHD. While it becomes more
593 internally-mixed as the enhanced fraction of more-hygroscopic mode and decreased
594 fraction of hydrophobic mode during the aging process. This highlights a dual
595 regulatory mechanism of mixing state and its potential impact on hygroscopic
596 distribution and CCN activity.

597 As χ increases, CN number concentrations (N_{CN}) first rise—driven by primary

设置了格式: 字体颜色: 自动设置

598 emissions and new particle formation—then decline due to condensation and
599 coagulation during aging. ~~Additionally, a logarithmic decreasing relationship~~
600 ~~between~~The critical diameter (D_{cri}) ~~and~~exhibits heightened sensitivity to minor χ ~~was~~
601 ~~identified~~fluctuations when $\chi < 0.5$. In contrast, for ~~both inland and coastal~~ particles;
602 ~~parameterized as~~ already characterized by internal mixing, further increases in χ (i.e.,
603 higher degrees of internal mixing) exert a negligible influence on $D_{\text{cri}} = -32.15\ln(\chi) +$
604 ~~84.71 (Pearson $R = -0.74$, $R^2 = 0.54$). This offers~~. Additionally, both environments show
605 ~~negative $D_{\text{cri}}-\chi$ correlations, but with distinct functional forms. We propose~~ a practical
606 approach ~~to estimate~~for estimating D_{cri} from χ , ~~applicable when the aerosol particles~~
607 ~~are not highly aged or when the internal mixing degree of aerosol particles is relatively~~
608 ~~low, serving as a~~ ~~general~~novel framework for integrating mixing state effects on CCN
609 activity in atmospheric models.

设置了格式: 字体颜色: 自动设置

610 Entropy-based analyses further support the covariation relationships between the
611 mixing state and N_{CCN} , especially for externally mixed aerosols. Current models often
612 oversimplify aerosol mixing states as purely internal or external (Stevens et al., 2019;
613 Bauer et al., 2013), the latter being particularly sensitive to organic matter (Ren et al.,
614 2018; Bhattu et al., 2015). Such simplifications introduce significant biases in N_{CCN}
615 estimation (Riemer et al., 2019; Ching et al., 2019). The χ - D_{cri} parameterization
616 proposed here offers a novel approach to reduce model complexity in representing
617 aerosol hygroscopicity and CCN activation, enabling more accurate simulations of
618 aerosol CCN capacity. It is expected mitigate the underestimation in CCN compared
619 with the complete external mixing assumption, while effectively alleviates the

620 overestimation that arises from applying the complete internal mixing assumption in
621 regions characterized by high external mixing (Zheng et al., 2021a). This advancement
622 improves our understanding of aerosol-cloud interactions (IPCC, 2021; Rosenfeld et al.,
623 2019), critical for refining climate effect assessments.

624 **Data availability**

625 All data used in the study are available at <https://doi.org/10.3974/geodb.2019.06.11.V1>
626 (Fan et al., 2019) and <http://doi.org/10.17632/3dx6pnx869.1> (Xu et al., 2021a).

627 **Author contributions**

628 RH and JR conceived the conceptual development of the paper. JR, FZ and WX directed
629 and performed the experiments with YW and LC. FZ and YS provided the dataset in
630 the inland site. JO, DC and CO provided the dataset in the coastal site. JR conducted
631 the data analysis and wrote the draft. All authors edited and commented on the various
632 sections of the paper.

633 **Competing interests**

634 The contact author has declared that none of the authors has any competing interests.

635 **Supporting Information**

636 Additional analysis results that were applied in this study. Example of calibration
637 results of HTDMA and CCN used in this study (Figure S1), mean values of the κ -PDF
638 for aerosols of five diameters (Figure S2), sensitivity of the hygroscopic parameter for
639 the group of the hygroscopic species on the mixing state index χ (Figure S3), time series

640 of the average per-particle species diversity $D\alpha$, the bulk population species diversity
641 $D\gamma$, and their affine ratio χ (Figure S4), diurnal trend of particle size, chemical mass
642 fraction and number fraction (NF) of hydrophobic and hygroscopic mode in IAP
643 (Figure S5) and in MHD (Figure S6), mixing state as a function of number fraction of
644 hydrophobic and hygroscopic mode (Figure S7), variation of the peak diameter (D_{peak})
645 with the mixing state index (Figure S8), particle number size distribution and mixing
646 state during new particle formation events (Figure S9), diurnal variation of χ and CN
647 concentration during winter and summer periods for 40 nm and 150 nm aerosols in
648 inland and for 35 nm and 165 nm aerosols in coastal site (Figure S10), relative change
649 of the critical diameter and CN concentration with the mixing state index χ (Figure S11)
650 (PDF).

651 **Acknowledgements**

652 This work was funded by the National Natural Science Foundation of China (NSFC)
653 under Grant No. 42525301, 42405118 and 42475112, the State Key Laboratory of
654 Loess Science, Institute of Earth Environment, Chinese Academy of Sciences
655 (SKLLQG2429), the Guangdong Natural Science Foundation (Grant No.
656 2024A1515011005). We thank all participants of the field campaign for their hard work
657 and sharing of the data.

658 **References**

659 Bhattu, D., Tripathi, S. N.: CCN closure study: Effects of aerosol chemical composition
660 and mixing state, *Journal of Geophysical Research: Atmospheres.*, 120(2), 766–
661 783, <https://doi.org/10.1002/2014JD021978>, 2015.

662 Bellouin, N., Quaas, J., Gryspeerdt, E., Kinne, S., Stier, P., Watson-Parris, D., Boucher,
663 O., Carslaw, K. S., Christensen, M., Daniau, A-L., Dufresne, J.-L., Feingold, G.,
664 Fiedler, S., Foster, P., Gettelman, A., Haywood, J. M., Lohmann, U., Malavelle, F.,
665 Mauritsen, T., McCoy, D. T., Schulz, M., Schwartz, S. E., Sourdeval, O.,
666 Storelvmo, T., Toll, V., Winker, D., and Stevens, B: Bounding global aerosol
667 radiative forcing of climate change, *Rev. Geophys.*, 58, e2019RG000660,
668 <https://doi.org/10.1029/2019RG000660>, 2020.

669 Bauer, S. E., Ault, A., Prather, K. A.: Evaluation of aerosol mixing state classes in the
670 GISS modelE-MATRIX climate model using single-particle mass spectrometry
671 measurements, *Journal of Geophysical Research: Atmospheres.*, 118, 9834–9844,
672 <https://doi.org/10.1002/jgrd.50700>, 2013.

673 Charlson, R. J., Schwartz, S. E., Hales, J. M., Cess, R. D., Coakley Jr, J. A., Hansen, J.
674 E., Hofmann, D. J.: Climate forcing by anthropogenic aerosols, *Science.*,
675 255(5043), 423–430, <https://doi.org/10.1126/science.255.5043.423>, 1992.

676 Chen, Y., Haywood, J., Wang, Y., Malavelle, F., Jordan, G., Partridge, D., Fieldsend, J.,
677 Leeuw, J. D., Schmidt, A., Cho, N., Oreopoulos, L., Platnick, S., Grosvenor, D.,
678 Field, P., Lohmann, U.: Machine learning reveals climate forcing from aerosols is
679 dominated by increased cloud cover, *Nature Geoscience.*, 15(8), 609–614,
680 <https://doi.org/10.1038/s41561-022-01027-9>, 2022a.

681 Chen, L., Zhang, F., Zhang, D., Wang, X., Song, W., Liu, J., Ren, J., Jiang, S., Li, X.,
682 and Li, Z.: Measurement report: Hygroscopic growth of ambient fine particles
683 measured at five sites in China, *Atmospheric Chemistry and Physics.*, 22, 6773-
684 6786, <https://doi.org/10.5194/acp-22-6773-2022>, 2022b.

685 Ching, J., Zaveri, R. A., Easter, R. C., Riemer, N., Fast, J. D.: A three-dimensional
686 sectional representation of aerosol mixing state for simulating optical properties
687 and cloud condensation nuclei, *Journal of Geophysical Research: Atmospheres.*,
688 121(10), 5912–5929, <https://doi.org/10.1002/2015JD024323>, 2016.

689 Ching, J., Fast, J., West, M., Riemer, N.: Metrics to quantify the importance of mixing
690 state for CCN activity, *Atmospheric Chemistry and Physics*, 17(12), 7445–7458,
691 <https://doi.org/10.5194/acp-17-7445-2017>, 2017.

692 Ching, J., Adachi, K., Zaizen, Y., Igarashi, Y., Kajino, M.: Aerosol mixing state revealed
693 by transmission electron microscopy pertaining to cloud formation and human
694 airway deposition, *npj Climate and Atmospheric Science*, 2(1), 22, [https://doi.org/](https://doi.org/10.1038/s41612-019-0081-9)
695 [10.1038/s41612-019-0081-9](https://doi.org/10.1038/s41612-019-0081-9), 2019.

696 Collins, D. B., Ault, A. P., Moffet, R. C., Ruppel, M. J., Cuadra-Rodriguez, L. A.,
697 Guasco, T. L., Corrigan, C. E., Pedler, B. E., Azam, F., Aluwihare, L. I., Bertram,
698 T. H., Roberts, G. C., Grassian, V. H., Prather, K. A.: Impact of marine
699 biogeochemistry on the chemical mixing state and cloud forming ability of nascent
700 sea spray aerosol, *Journal of Geophysical Research: Atmospheres*, 118(15), 8553–
701 8565, <https://doi.org/10.1002/jgrd.50598>, 2013.

702 Cheung, H. C., Chou, C. C. K., Lee, C. S. L., Kuo, W. C., Chang, S. C.: Hygroscopic
703 properties and cloud condensation nuclei activity of atmospheric aerosols under
704 the influences of Asian continental outflow and new particle formation at a coastal
705 site in eastern Asia, *Atmospheric Chemistry and Physics*, 20(10), 5911–5922,
706 <https://doi.org/10.5194/acp-20-5911-2020>, 2020.

707 Cai, J., Chu, B., Yao, L., Yan, C., Heikkinen, L. M., Zheng, F., Li, C., Fan, X., Zhang,
708 S., Yang, D., Wang, Y., Kokkonen, T. V., Chan, T., Zhou, Y., Dada, L., Liu, Y., He,
709 H., Paasonen, P., Kujansuu, J. T., Petäjä, T., Mohr, C., Kangasluoma, J., Bianchi,
710 F., Sun, Y., Croteau, P. L., Worsnop, D. R., Kerminen, V. M., Du, W., Kulmala, M.,
711 & Daellenbach, K. R.: Size-segregated particle number and mass concentrations
712 from different emission sources in urban Beijing, *Atmospheric Chemistry and*
713 *Physics*, 20(21), 12721–12740, <https://doi.org/10.5194/acp-20-12721-2020>, 2020.

714 Dusek, U., Frank, G. P., Hildebrandt, L., Curtius, J., Schneider, J., Walter, S., Chand,
715 D., Drewnick, F., Hings, S., Jung, D., Borrmann, S., Andreae, M. O.: Size matters
716 more than chemistry for cloud-nucleating ability of aerosol particles, *Science*, 312
717 (5778), 1375–1378, <https://doi.org/10.1126/science.1125261>, 2006.

718 DeCarlo, P. F., Kimmel, J. R., Trimborn, A., Northway, M. J., Jayne, J. T., Aiken, A. C.,
719 Gonin, M., Fuhrer, K., Horvath, T., Docherty, K. S., Worsnop, D. R., Jimenez, J.
720 L.: Field-deployable, high-resolution, time of-flight aerosol mass spectrometer,
721 *Analytical Chemistry*, 78, 8281–8289, <https://doi.org/10.1021/ac061249n>, 2006.

722 Ervens, B., Cubison, M. J., Andrews, E., Feingold, G., Ogren, J. A., Jimenez, J. L.,
723 Quinn, P. K., Bates, T. S., Wang, J., Zhang, Q., Coe, H., Flynn, M., Allan, J. D.:
724 CCN predictions using simplified assumptions of organic aerosol composition and
725 mixing state: a synthesis from six different locations, *Atmospheric Chemistry and*
726 *Physics*, 10(10), 4795–4807, <https://doi.org/10.5194/acp-10-4795-2010>, 2010.

727 Fierce, L., Onasch, T. B., Cappa, C. D., Mazzoleni, C., China, S., Bhandari, J.,
728 Davidovits, P., Fischer, D. A., Helgestad, T., Lambe, A. T., et al.: Radiative
729 absorption enhancements by black carbon controlled by particle-to-particle
730 heterogeneity in composition, *P. Natl. Acad. Sci. USA*, 117, 5196–5203,
731 <https://doi.org/10.1073/pnas.1919723117>, 2020.

732 Fan, X., Liu, J., Zhang, F., Chen, L., Collins, D., Xu, W., Jin, X., Ren, J., Wang, Y., Wu,
733 H., Li, S., Sun, Y., Li, Z.: Contrasting size-resolved hygroscopicity of fine particles
734 derived by HTDMA and HR-ToF-AMS measurements between summer and
735 winter in Beijing: the impacts of aerosol aging and local emissions, *Atmospheric*
736 *Chemistry and Physics*, 20(2), 915–929, <https://doi.org/10.5194/acp-20-915-2020>,
737 2020.

738 Gysel, M., Mcfiggans, G. B., Coe, H.: Inversion of tandem differential mobility
739 analyser (TDMA) measurements, *Journal of Aerosol Science*, 40(2), 134–151,
740 <https://doi.org/10.1016/j.jaerosci.2008.07.013>, 2009.

741 Hughes, M., Kodros, J. K., Pierce, J. R., West, M., Riemer, N.: Machine learning to
742 predict the global distribution of aerosol mixing state metrics, *Atmosphere*, 9(1),
743 15, <https://doi.org/10.3390/atmos9010015>, 2018.

744 Huang, R. J., Zhang, Y., Bozzetti, C., Ho, K. F., Cao, J. J., Han, Y., Daellenbach, K. R.,
745 Slowik, J. G., Platt, S. M., Canonaco, F., Zotter, P., Wolf, R., Pieber, S. M., Bruns,
746 E. A., Crippa, M., Ciarelli, G., Piazzalunga, A., Schwikowski, M., Abbaszade, G.,

747 Schnelle-Kreis, J., Zimmermann, R., An, Z., Szidat, S., Baltensperger, U., Haddad,
748 I. E., Prévôt, A. S.: High secondary aerosol contribution to particulate pollution
749 during haze events in China, *Nature.*, 514(7521), 218–222, [https://doi.org/](https://doi.org/10.1038/nature13774)
750 10.1038/nature13774, 2014.

751 IPCC. Summary for Policymakers. In *Climate Change 2021: The Physical Science*
752 *Basis. Contribution of Working Group I to the Sixth Assessment Report of the*
753 *Intergovernmental Panel on Climate Change*; Cambridge University Press:
754 Cambridge, United Kingdom and New York, NY, USA, 2021.

755 Liu, P., Song, M., Zhao, T., Gunthe, S. S., Ham, S., He, Y., Qin, Y., Gong, Z., Amorim,
756 C. J., Bertram, K. A., Martin, S. T.: Resolving the mechanisms of hygroscopic
757 growth and cloud condensation nuclei activity for organic particulate matter,
758 *Nature communications.*, 9(1), 4076, [https://doi.org/10.1038/s41467-018-06622-](https://doi.org/10.1038/s41467-018-06622-2)
759 2, 2018.

760 Liu, J., Zhang, F., Ren, J., Chen, L., Zhang, A., Wang, Z., Zou, S., Xu, H., Yue, X.: The
761 evolution of aerosol mixing state derived from a field campaign in Beijing:
762 implications for particle aging timescales in urban atmospheres, *Atmospheric*
763 *Chemistry and Physics.*, 25(9), 5075–5086, [https://doi.org/10.5194/acp-25-5075-](https://doi.org/10.5194/acp-25-5075-2025)
764 2025, 2025.

765 Liu, Y., Lin, T., Zhang, J., Wang, F., Huang, Y., Wu, X., Ye, H., Zhang, G., Cao, X., and
766 de Leeuw, G.: Opposite effects of aerosols and meteorological parameters on
767 warm clouds in two contrasting regions over eastern China, *Atmospheric*
768 *Chemistry and Physics.*, 24, 4651–4673, [https://doi.org/10.5194/acp-24-4651-](https://doi.org/10.5194/acp-24-4651-2024)
769 2024, 2024.

770 Lance, S., Nenes, A., Medina, J., Smith, J. N.: Mapping the operation of the DMT
771 continuous flow CCN counter, *Aerosol Science and Technology.*, 40(4), 242–254,
772 <https://doi.org/10.1080/02786820500543290>, 2006.

773 Manavi, S. E. I., Aktypis, A., Siouti, E., Skyllakou, K., Myriokefalitakis, S., Kanakidou,
774 M., Pandis, S. N.: Atmospheric aerosol spatial variability: Impacts on air quality
775 and climate change, *One Earth.*, 8(3),

776 <https://doi.org/10.1016/j.oneear.2025.101237>, 2025.

777 Ovadnevaite, J., Ceburnis, D., Leinert, S., Dall'Osto, M., Canagaratna, M., O'Doherty,
778 S., Berresheim, H., O'Dowd, C.: Submicron NE Atlantic marine aerosol chemical
779 composition and abundance: Seasonal trends and air mass categorization, *Journal*
780 *of Geophysical Research: Atmospheres.*, 119, 11850–11863,
781 <https://doi.org/10.1002/2013JD021330>, 2014.

782 Petters, M. D., Kreidenweis, S. M.: A single parameter representation of hygroscopic
783 growth and cloud condensation nucleus activity, *Atmospheric Chemistry and*
784 *Physics.*, 7(8), 1961–1971, <https://doi.org/10.5194/acp-7-1961-2007>, 2007.

785 Padró, L. T., Moore, R. H., Zhang, X., Rastogi, N., Weber, R. J., and Nenes, A.: Mixing
786 state and compositional effects on CCN activity and droplet growth kinetics of
787 size-resolved CCN in an urban environment, *Atmospheric Chemistry and Physics.*,
788 2012, 12, 10239–10255, <https://doi.org/10.5194/acp-12-10239-2012>, 2012.

789 Rosenfeld, D., Zhu, Y., Wang, M., Zheng, Y., Goren, T., Yu, S.: Aerosol- driven droplet
790 concentrations dominate coverage and water of oceanic low-level clouds, *Science.*,
791 363(6427), <https://doi.org/10.1126/science.aay4194>, 2019.

792 Riemer, N., Ault, A. P., West, M., Craig, R. L., Curtis, J. H.: Aerosol mixing state:
793 Measurements, modeling, and impacts, *Reviews of Geophysics.*, 57(2), 187–249,
794 <https://doi.org/10.1029/2018RG000615>, 2019.

795 Ren, J., Zhang, F., Wang, Y., Collins, D., Fan, X., Jin, X., Xu, W., Sun, Y., Cribb, M.,
796 Li, Z.: Using different assumptions of aerosol mixing state and chemical
797 composition to predict CCN concentrations based on field measurements in urban
798 Beijing, *Atmospheric Chemistry and Physics.*, 18(9), 6907–6921,
799 <https://doi.org/10.5194/acp-18-6907-2018> 2018.

800 Ramachandran, S., Srivastava, R.: Mixing states of aerosols over four environmentally
801 distinct atmospheric regimes in Asia: coastal, urban, and industrial locations
802 influenced by dust, *Environmental Science and Pollution Research.*, 23, 11109–
803 11128, <https://doi.org/10.1007/s11356-016-6254-8>, 2016.

804 Ren, J., Zhang, F., Chen, L., Cao, G., Liu, M., Li, X., Wu, H., Cheng, Y., and Li, Z.:

805 Identifying the hygroscopic properties of fine aerosol particles from diverse
806 sources in urban atmosphere and the applicability in prediction of cloud nuclei,
807 *Atmos. Environ.*, 298, 119615, <https://doi.org/10.1016/j.atmosenv.2023.119615>,
808 2023.

809 Riemer, N. and West, M.: Quantifying aerosol mixing state with entropy and diversity
810 measures, *Atmospheric Chemistry and Physics.*, 13, 11423–11439,
811 <https://doi.org/10.5194/acp-13-11423-2013>, 2013.

812 Rose, D., Gunthe, S. S., Mikhailov, E., Frank, G. P., Dusek, U., Andreae, M. O., Pöschl,
813 U.: Calibration and measurement uncertainties of a continuous-flow cloud
814 condensation nuclei counter (DMT-CCNC): CCN activation of ammonium sulfate
815 and sodium chloride aerosol particles in theory and experiment, *Atmospheric
816 Chemistry and Physics.*, 8(5), 1153–1179, [https://doi.org/10.5194/acp-8-1153-
817 2008](https://doi.org/10.5194/acp-8-1153-2008), 2008.

818 Shrivastava, M., Cappa, C. D., Fan, J., Goldstein, A. H., Guenther, A. B., Jimenez, J.
819 L., Kuang, C., Laskin, A., Martin, S. T., Ng, N. L., Petaja, T., Pierce, J. R., Rasch,
820 P. J., Roldin, P., Seinfeld, J. H., Shilling, J., Smith, J. N., Thornton, J. A., Volkamer,
821 R., Wang, J., Worsnop, D. R., Zaveri, R. A., Zelenyuk, A., Zhang, Q.: Recent
822 advances in understanding secondary organic aerosol: Implications for global
823 climate forcing, *Reviews of Geophysics.*, 55(2), 509–559,
824 <https://doi.org/10.1002/2016RG000540>, 2017.

825 Stevens, R., and Dastoor, A.: A Review of the Representation of Aerosol Mixing State
826 in Atmospheric Models, *Atmosphere.*, 10, 168,
827 <https://doi.org/10.3390/atmos10040168>, 2019.

828 Spitieri, C., Gini, M., Gysel-Ber, M., and Eleftheriadis, K.: Annual cycle of
829 hygroscopic properties and mixing state of the suburban aerosol in Athens, Greece,
830 *Atmospheric Chemistry and Physics.*, 23, 235–249, [https://doi.org/10.5194/acp-
831 23-235-2023](https://doi.org/10.5194/acp-23-235-2023), 2023.

832 Sotiropoulou, R. E. P., Nenes, A., Adams, P. J., Seinfeld, J. H.: Cloud condensation
833 nuclei prediction error from application of Köhler theory: Importance for the

834 aerosol indirect effect, *Journal of Geophysical Research: Atmospheres.*, 112(D12),
835 <https://doi.org/10.1029/2006JD007834>, 2007.

836 Schill, S. R., Collins, D. B., Lee, C., Morris, H. S., Novak, G. A., Prather, K. A., Quinn,
837 P. K., Sultana, C. M., Tivanski, A. V., Zimmermann, K., Cappa, C. D., Bertram, T.
838 H.: The impact of aerosol particle mixing state on the hygroscopicity of sea spray
839 aerosol, *ACS central science.*, 1(3), 132-141,
840 <https://doi.org/10.1021/acscentsci.5b00174>, 2015.

841 Shi, Z., Vu, T., Kotthaus, S., Harrison, R. M., Grimmond, S., Yue, S., Zhu, T., Lee, J.,
842 Han, Y., Demuzere, M., Dunmore, R. E., Ren, L., Liu, D., Wang, Y., Wild, O.,
843 Allan, J., Acton, W. J., Barlow, J., Barratt, B., Beddows, D., Bloss, W. J., Calzolari,
844 G., Carruthers, D., Carslaw, D. C., Chan, Q., Chatzidiakou, L., Chen, Y., Crilley,
845 L., Coe, H., Dai, T., Doherty, R., Duan, F., Fu, P., Ge, B., Ge, M., Guan, D.,
846 Hamilton, J. F., He, K., Heal, M., Heard, D., Hewitt, C. N., Hollaway, M., Hu, M.,
847 Ji, D., Jiang, X., Jones, R., Kalberer, M., Kelly, F. J., Kramer, L., Langford, B.,
848 Lin, C., Lewis, A. C., Li, J., Li, W., Liu, H., Liu, J., Loh, M., Lu, K., Lucarelli, F.,
849 Mann, G., McFiggans, G., Miller, M. R., Mills, G., Monk, P., Nemitz, E., O'Connor,
850 F., Ouyang, B., Palmer, P. I., Percival, C., Popoola, O., Reeves, C., Rickard, A. R.,
851 Shao, L., Shi, G., Spracklen, D., Stevenson, D., Sun, Y., Sun, Z., Tao, S., Tong, S.,
852 Wang, Q., Wang, W., Wang, X., Wang, X., Wang, Z., Wei, L., Whalley, L., Wu, X.,
853 Wu, Z., Xie, P., Yang, F., Zhang, Q., Zhang, Y., Zhang, Y., and Zheng, M.:
854 Introduction to the special issue "In-depth study of air pollution sources and
855 processes within Beijing and its surrounding region (APHH-Beijing)",
856 *Atmospheric Chemistry and Physics.*, 19, 7519–7546, [https://doi.org/10.5194/acp-](https://doi.org/10.5194/acp-19-7519-2019)
857 [19-7519-2019](https://doi.org/10.5194/acp-19-7519-2019), 2019.

858 Stokes, R. H., Robinson, R. A.: Interactions in aqueous nonelectrolyte solutions. I.
859 Solute-Solvent equilibria, *Journal of Physical Chemistry.*, 70(7), 2126–2130,
860 <https://doi.org/10.1021/j100879a010>, 1966.

861 Tao, J., Kuang, Y., Ma, N., Hong, J., Sun, Y., Xu, W., Zhang, Y., He, Y., Luo, Q., Xie,
862 L., Su, H., and Cheng, Y.: Secondary aerosol formation alters CCN activity in the

863 North China Plain, *Atmospheric Chemistry and Physics*, 21, 7409–7427,
864 <https://doi.org/10.5194/acp-21-7409-2021>, 2021.

865 Tao, J., Luo, B., Xu, W., Zhao, G., Xu, H., Xue, B., Zhai, M., Xu, W., Zhao, H., Ren,
866 S., Zhou, G., Liu, L., Kuang, Y., and Sun, Y.: Markedly different impacts of
867 primary emissions and secondary aerosol formation on aerosol mixing states
868 revealed by simultaneous measurements of CCNC, H(V)TDMA, and SP2,
869 *Atmospheric Chemistry and Physics*, 24, 9131–9154, [https://doi.org/10.5194/acp-](https://doi.org/10.5194/acp-24-9131-2024)
870 [24-9131-2024](https://doi.org/10.5194/acp-24-9131-2024), 2024.

871 Virtanen, A., Joutsensaari, J., Kokkola, H., Partridge, G. D., Blichner, S., Seland, Ø.,
872 Holopainen, E., Tovazzi, E., Lipponen, A., Mikkonen, S., Leskinen, A., Hyvärinen,
873 A., Zieger, P., Krejci, R., Ekman, A. M. L., Riipinen, I., Quaas, J., Romakkaniemi,
874 S.: High sensitivity of cloud formation to aerosol changes, *Nature Geoscience*, 1–
875 7, <https://doi.org/10.1038/s41561-025-01662-y>, 2025.

876 Winkler, P.: The growth of atmospheric aerosol particles as a function of the relative
877 humidity—II. An improved concept of mixed nuclei, *Journal of Aerosol Science*,
878 4(5), 373–387, [https://doi.org/10.1016/0021-8502\(73\)90027-X](https://doi.org/10.1016/0021-8502(73)90027-X), 1973.

879 Wang, J., Cubison, M. J., Aiken, A. C., Jimenez, J. L., Collins, D. R.: The importance
880 of aerosol mixing state and size-resolved composition on CCN concentration and
881 the variation of the importance with atmospheric aging of aerosols, *Atmospheric*
882 *Chemistry and Physics*, 10(15), 7267–7283, [https://doi.org/10.5194/acp-10-7267-](https://doi.org/10.5194/acp-10-7267-2010)
883 [2010](https://doi.org/10.5194/acp-10-7267-2010), 2010.

884 Wang, Y., Li, Z., Zhang, R., Jin, X., Xu, W., Fan, X., et al.: Distinct ultrafine- and
885 accumulation-mode particle properties in clean and polluted urban environments,
886 *Geophysical Research Letters*, 46, 10,918–10,925,
887 <https://doi.org/10.1029/2019GL084047>, 2019.

888 Xu, W., Ovadnevaite, J., Fossum, K. N., Lin, C., Huang, R. J., Ceburnis, D., O’Dowd,
889 C.: Sea spray as an obscured source for marine cloud nuclei, *Nature Geoscience*,
890 15(4), 282–286, <https://doi.org/10.1038/s41561-022-00917-2>, 2022.

891 Xu, W., Ovadnevaite, J., Fossum, K. N., Huang, R. J., Huang, D., Zhong, H., Gu, Y.,

892 Lin, C., Huang, C., O'Dowd, C., Ceburnis, D.: Condensation of organic-inorganic
893 vapours governs the production of ultrafine secondary marine cloud nuclei,
894 *Communications Earth & Environment.*, 5(1), 359,
895 <https://doi.org/10.1038/s43247-024-01519-z>, 2024.

896 Xu, W., Ovadnevaite, J., Fossum, K. N., Lin, C., Huang, R. J., O'Dowd, C., Ceburnis,
897 D.: Aerosol hygroscopicity and its link to chemical composition in the coastal
898 atmosphere of Mace Head: marine and continental air masses, *Atmospheric*
899 *Chemistry and Physics.*, 20(6), 3777–3791, [https://doi.org/10.5194/acp-20-3777-](https://doi.org/10.5194/acp-20-3777-2020)
900 2020, 2020.

901 Xu, W., Ovadnevaite, J., Fossum, K. N., Lin, C., Huang, R.-J., O'Dowd, C., Ceburnis,
902 D.: Seasonal trends of aerosol hygroscopicity and mixing state in clean marine and
903 polluted continental air masses over the Northeast Atlantic, *Journal of Geophysical*
904 *Research: Atmospheres.*, 126, e2020JD033851,
905 <https://doi.org/10.1029/2020JD033851>, 2021a.

906 Xu, W., Sun, Y., Wang, Q., Zhao, J., Wang, J., Ge, X., Xie, C., Zhou, W., Du, W., Li, J.,
907 Fu, P., Wang, Z., Worsnop, D. R., Coe, H.: Changes in aerosol chemistry from
908 2014 to 2016 in winter in Beijing: Insights from high-resolution aerosol mass
909 spectrometry, *Journal of Geophysical Research: Atmospheres.*, 124, 1132–1147,
910 <https://doi.org/10.1029/2018JD029245>, 2019.

911 Xie, C., He, Y., Lei, L., Zhou, W., Liu, J., Wang, Q., Xu, W., Qiu, Y., Zhao, J., Sun, J.,
912 Li, L., Li, M., Zhou, Z., Fu, P., Wang, Z., Sun, Y.: Contrasting mixing state of black
913 carbon-containing particles in summer and winter in Beijing, *Environmental*
914 *Pollution.*, 263, 114455, <https://doi.org/10.1016/j.envpol.2020.114455>, 2020.

915 Xu, W., Fossum, K. N., Ovadnevaite, J., Lin, C., Huang, R. J., O'Dowd, C., Ceburnis,
916 D.: The impact of aerosol size-dependent hygroscopicity and mixing state on the
917 cloud condensation nuclei potential over the north-east Atlantic, *Atmospheric*
918 *Chemistry and Physics.*, 21(11), 8655–8675, [https://doi.org/10.5194/acp-21-8655-](https://doi.org/10.5194/acp-21-8655-2021)
919 2021, 2021b.

920 Ye, Q., Gu, P., Li, H. Z., Robinson, E. S., Lipsky, E. M., Kaltsonoudis, C., Lee, A. K.

921 Y., Apte, J. S., Robinson, A. L., Sullivan, R. C., Presto, A. A., Donahue, N. M.:
922 Spatial variability of sources and mixing state of atmospheric particles in a
923 metropolitan area, *Environmental Science & Technology.*, 52, 6807–6815,
924 <https://doi.org/10.1021/acs.est.8b01011>, 2018.

925 Yuan, L., and Zhao, C.: Quantifying particle-to-particle heterogeneity in aerosol
926 hygroscopicity, *Atmospheric Chemistry and Physics.*, 23, 3195–3205,
927 <https://doi.org/10.5194/acp-23-3195-2023>, 2023.

928 Yang, F., Chen, H., Du, J., Yang, X., Gao, S., Chen, J., Geng, F.: Evolution of the mixing
929 state of fine aerosols during haze events in Shanghai, *Atmospheric Research.*, 104:
930 193-201, <https://doi.org/10.1016/j.atmosres.2011.10.005>, 2012.

931 Zheng, Z., Curtis, J. H., Yao, Y., Gasparik, J. T., Anantharaj, V. G., Zhao, L., West, M.,
932 Riemer, N.: Estimating submicron aerosol mixing state at the global scale with
933 machine learning and Earth system modeling, *Earth and Space Science.*, 8(2),
934 e2020EA001500, <https://doi.org/10.1029/2020EA001500>, 2021a.

935 Zheng, Z., West, M., Zhao, L., Ma, P.-L., Liu, X., and Riemer, N.: Quantifying the
936 structural uncertainty of the aerosol mixing state representation in a modal model,
937 *Atmospheric Chemistry and Physics.*, 21, 17727–17741,
938 <https://doi.org/10.5194/acp-21-17727-2021>, 2021b.

939 Zhao, G., Tan, T., Zhu, Y., Hu, M., and Zhao, C.: Method to quantify black carbon
940 aerosol light absorption enhancement with a mixing state index, *Atmospheric
941 Chemistry and Physics.*, 21, 18055–18063, [https://doi.org/10.5194/acp-21-18055-](https://doi.org/10.5194/acp-21-18055-2021)
942 2021, 2021.

943 Zdanovskii, A.: New methods for calculating solubilities of electrolytes in
944 multicomponent systems, *Zh. Fiz. Khim. C*, 22, 1475–1485, 1948.

945 Zhong, H., Huang, R. J., Lin, C., Xu, W., Duan, J., Gu, Y., Huang, W., Ni, H.; Zhu, C.,
946 You, Y., Wu, Y., Zhang, R., Ovadnevaite, J., Ceburnis, D., O'Dowd, C.:
947 Measurement report: On the contribution of long-distance transport to the
948 secondary aerosol formation and aging, *Atmospheric Chemistry and Physics.*, 22,
949 9513–9524, <https://doi.org/10.5194/acp-22-9513-2022>, 2022.